Compact tunable silicon photonic differential-equation solver for general linear time-invariant systems

Jiayang Wu,[1] Pan Cao,[1] Xiaofeng Hu,[1] Xinhong Jiang,[1] Ting Pan,[1] Yuxing Yang,[1] Ciyuan Qiu,[1] Christine Tremblay,[2] and Yikai Su[1,*]

[1]*State Key Lab of Advanced Optical Communication Systems and Networks, Department of Electronic Engineering, Shanghai Jiao Tong University, Shanghai 200240, China*

[2]*Laboratoire de Technologies de Réseaux, École de Technologie Supérieure, Montreal, Canada*

[*]*yikaisu@sjtu.edu.cn*

Abstract: We propose and experimentally demonstrate an all-optical temporal differential-equation solver that can be used to solve ordinary differential equations (ODEs) characterizing general linear time-invariant (LTI) systems. The photonic device implemented by an add-drop microring resonator (MRR) with two tunable interferometric couplers is monolithically integrated on a silicon-on-insulator (SOI) wafer with a compact footprint of ~60 μm × 120 μm. By thermally tuning the phase shifts along the bus arms of the two interferometric couplers, the proposed device is capable of solving first-order ODEs with two variable coefficients. The operation principle is theoretically analyzed, and system testing of solving ODE with tunable coefficients is carried out for 10-Gb/s optical Gaussian-like pulses. The experimental results verify the effectiveness of the fabricated device as a tunable photonic ODE solver.

OCIS codes: (130.3120) Integrated optics devices; (070.1170) Analog optical signal processing; (230.5750) Resonators.

References and links

1. L. Venema, "Photonic technologies," Nature **424**(6950), 809 (2003).
2. F. Liu, T. Wang, L. Qiang, T. Ye, Z. Zhang, M. Qiu, and Y. Su, "Compact optical temporal differentiator based on silicon microring resonator," Opt. Express **16**(20), 15880–15886 (2008).
3. N. K. Berger, B. Levit, B. Fischer, M. Kulishov, D. V. Plant, and J. Azaña, "Temporal differentiation of optical signals using a phase-shifted fiber Bragg grating," Opt. Express **15**(2), 371–381 (2007).
4. M. Ferrera, Y. Park, L. Razzari, B. E. Little, S. T. Chu, R. Morandotti, D. J. Moss, and J. Azaña, "On-chip CMOS-compatible all-optical integrator," Nat. Commun. **1**(29), 29 (2010).
5. N. Quoc Ngo, "Design of an optical temporal integrator based on a phase-shifted fiber Bragg grating in transmission," Opt. Lett. **32**(20), 3020–3022 (2007).
6. J. Azaña, "Proposal of a uniform fiber Bragg grating as an ultrafast all-optical integrator," Opt. Lett. **33**(1), 4–6 (2008).
7. R. Slavík, Y. Park, N. Ayotte, S. Doucet, T. J. Ahn, S. LaRochelle, and J. Azaña, "Photonic temporal integrator for all-optical computing," Opt. Express **16**(22), 18202–18214 (2008).
8. R. Ashrafi and J. Azaña, "Terahertz bandwidth all-optical Hilbert transformers based on long-period gratings," Opt. Lett. **37**(13), 2604–2606 (2012).
9. L. Zhuang, M. R. Khan, W. Beeker, A. Leinse, R. Heideman, and C. Roeloffzen, "Novel microwave photonic fractional Hilbert transformer using a ring resonator-based optical all-pass filter," Opt. Express **20**(24), 26499–26510 (2012).
10. G. F. Simmons, *Differential Equations With Applications and Historical Notes* (McGraw-Hill, 1991), Chap. 1.
11. A. V. Oppenheim, A. S. Willsky, and S. Hamid, *Signals and Systems* (Prentice-Hall, 1996), Chap. 2.
12. K. Y. Yun, P. A. Beerel, V. Vakilotojar, A. E. Dooply, and J. Arceo, "The design and verification of a high-performance low-control-overhead asynchronous differential equation solver," IEEE Trans. VLIS Syst. **6**(4), 643–655 (1998).
13. S. Tan, Z. Wu, L. Lei, S. Hu, J. Dong, and X. Zhang, "All-optical computing system for solving differential equations based on optical intensity differentiator," Opt. Express **21**(6), 7008–7013 (2013).
14. S. Tan, L. Xiang, J. Zou, Q. Zhang, Z. Wu, Y. Yu, J. Dong, and X. Zhang, "High-order all-optical differential equation solver based on microring resonators," Opt. Lett. **38**(19), 3735–3738 (2013).

#217421 - $15.00 USD Received 21 Jul 2014; revised 17 Sep 2014; accepted 18 Sep 2014; published 17 Oct 2014

15. T. Yang, J. Dong, L. Lu, L. Zhou, A. Zheng, X. Zhang, and J. Chen, "All-optical differential equation solver with constant-coefficient tunable based on a single microring resonator," Sci. Rep. **4**, 5581 (2014).
16. A. V. Oppenheim, A. S. Willsky, and S. Hamid, *Signals and Systems* (Prentice-Hall, 1996), Chap. 4.
17. C. Manolatou, M. Khan, S. Fan, P. Villeneuve, H. Haus, and J. Joannopoulos, "Coupling of modes analysis of resonant channel add-drop filters," IEEE J. Quantum Electron. **35**(9), 1322–1331 (1999).
18. L. Chen, N. Sherwood-Droz, and M. Lipson, "Compact bandwidth-tunable microring resonators," Opt. Lett. **32**(22), 3361–3363 (2007).
19. P. Koonath, T. Indukuri, and B. Jalali, "Monolithic 3-D silicon photonics," J. Lightwave Technol. **24**(4), 1796–1804 (2006).
20. P. J. Winzer and R. J. Essiambre, "Advanced optical modulation formats," Proc. IEEE **94**(5), 952–985 (2006).
21. J. Wu, P. Cao, X. Hu, T. Wang, M. Xu, X. Jiang, F. Li, L. Zhou, and Y. Su, "Nested configuration of silicon microring resonator with multiple coupling regimes," IEEE Photon. Technol. Lett. **25**(6), 580–583 (2013).

1. Introduction

After decades of development and miniaturization, the integrated electronic devices for computing and information processing are rapidly approaching their fundamental speed limitations [1]. In comparison with the electronic counterpart, all-optical computing and information processing based on photonic devices may show advantages in high-speed processing by overcoming the bandwidth bottleneck. In recent years, a number of photonic devices performing real-time information processing equivalent to electronic processors have been proposed and demonstrated, such as differentiators [2, 3], integrators [4–7], and Hilbert transformers [8, 9].

Differential equations model and govern fundamental phenomena and applied processes in virtually any field of science and engineering [10]. As the fundamental differential equations, constant-coefficient linear ordinary differential equations (ODEs) are widely employed in modeling of linear time-invariant (LTI) systems [11]. Solving ODEs plays a prominent role in real-time information processing [10]. As expected, all-optical ODE solvers could potentially offer processing bandwidths that are orders of magnitude larger than their electronic counterparts [12]. An optical ODE solving system based on semiconductor optical amplifiers (SOAs) and optical filters was proposed in previous work [13]. Precise control of time delay and additional optical pump are necessary for the system implemented by discrete devices. On the other hand, an integrated scheme using the drop ports of add-drop microring resonators (MRRs) was reported in [14, 15]. The ODE solvers can be used to solve simplified ODEs without derivative terms of input signal, while solving ODEs with various orders of derivative terms of input signal is needed to characterize general LTI systems in practical applications.

In this paper, we propose and experimentally demonstrate a tunable on-chip all-optical ODE solver for general LTI systems. The proposed ODE solver is based on a compact add-drop MRR with two tunable interferometric couplers. The device is monolithically integrated on a silicon-on-insulator (SOI) wafer through a fabrication process compatible to the state-of-art complementary metal-oxide semiconductor (CMOS) technology. By thermally tuning the phase shifts along the bus arms of the two interferometric couplers, the proposed device can be used to solve first-order ODEs with two variable coefficients. System testing of solving ODE with tunable coefficients using the fabricated device is performed with 10-Gb/s optical Gaussian-like pulses, and an excellent agreement between the numerical solutions of the ODE and the experimental results is obtained. The proposed ODE solver offers a competitive edge to solve general ODEs including various orders of derivative terms of input signal, which can be used in the modeling and characterization of general LTI systems.

2. Operation principle

Based on the classical theory of signals and systems, all LTI systems can be described by a linear constant-coefficient ODE normalized as [16]:

$$\frac{d^n y(t)}{dt^n} + \sum_{i=0}^{n-1} a_i \frac{d^i y(t)}{dt^i} = \sum_{k=0}^{m} b_k \frac{d^k x(t)}{dt^k}, \tag{1}$$

#217421 - $15.00 USD Received 21 Jul 2014; revised 17 Sep 2014; accepted 18 Sep 2014; published 17 Oct 2014

where $x(t)$ is the function representing a system input signal, and $y(t)$ is the function representing the solution of the ODE as the system output. a_i (i = 0, 1, 2…, n–1) and b_k (k = 0, 1, 2…, m) are the constant coefficients of the i^{th} order derivative of $y(t)$ and the k^{th} order derivative of $x(t)$, respectively. Note that $a_i \geq 0$ (i = 0, 1, 2…, n–1) and $m \leq n$ should be satisfied to ensure the causality and stability for practical systems. For first-order LTI systems, Eq. (1) can be simplified to:

$$\frac{dy(t)}{dt} + a_0 y(t) = b_1 \frac{dx(t)}{dt} + b_0 x(t). \tag{2}$$

After Fourier transformation from Eq. (2), the spectral transfer function can be given by [16]:

$$H(\omega) = \frac{b_1 j\omega + b_0}{j\omega + a_0} \propto \frac{j\omega + b_0 / b_1}{j\omega + a_0}, \tag{3}$$

where $j = \sqrt{-1}$, and ω is the angular frequency variable. Compared to the formula in [14, 15], the ODE in Eq. (2) includes an additional first-order derivative term of input signal $b_1 dx(t)/dt$, allowing for a more general and versatile modeling of LTI systems. The maximum transmission of the filter in Eq. (3) is normalized to 1 since it does not affect the shape of the output signal. Given that there are other amplifications or attenuations in practical processing process, the difference in amplitude can be further compensated.

For a practical first-order optical filter implemented by an add-drop MRR, the spectral transfer function of the through port around any given resonance can be expressed as [17]:

$$T(\omega) = \frac{j(\omega - \omega_0) + (\frac{\omega_0}{2Q_i} + \frac{\omega_0}{2Q_{e2}} - \frac{\omega_0}{2Q_{e1}})}{j(\omega - \omega_0) + (\frac{\omega_0}{2Q_i} + \frac{\omega_0}{2Q_{e1}} + \frac{\omega_0}{2Q_{e2}})}, \tag{4}$$

where ω_0 is the resonance frequency of the MRR, Q_i, Q_{e1}, and Q_{e2} are the quality factors induced by the internal cavity loss, the external coupling between the microring and the input waveguide, and the external coupling between the microring and the drop waveguide, respectively. According to the coupled mode theory, the three quality factors can be given by [18, 19]:

$$\begin{aligned} Q_i &= \omega_0 n_g L / \left[c \ln(1-\eta) \right] \\ Q_{e1} &= \omega_0 n_g L / \left[c \ln(1-\kappa_1) \right], \\ Q_{e2} &= \omega_0 n_g L / \left[c \ln(1-\kappa_2) \right] \end{aligned} \tag{5}$$

where n_g is the group index, L is the circumference of the MRR, c is the speed of light in vacuum, η is the round-trip intrinsic power loss, κ_1 is the power coupling coefficient between the microring and the input waveguide, and κ_2 is the power coupling coefficient between the microring and the drop waveguide. $T(\omega)$ in Eq. (4) shows an agreement with normalized $H(\omega)$ in Eq. (3). For an input optical signal with a carrier frequency of ω_0, the temporal ODE corresponding to $T(\omega)$ after inverse Fourier transformation is [16]:

$$\frac{dy(t)}{dt} e^{j\omega_0 t} + a_0 [y(t) e^{j\omega_0 t}] = \frac{dx(t)}{dt} e^{j\omega_0 t} + b_0 [x(t) e^{j\omega_0 t}], \tag{6}$$

where $x(t)e^{j\omega_0 t}$ and $y(t)e^{j\omega_0 t}$ are the functions representing the input and output optical signals, respectively, with $x(t)$ and $y(t)$ denoting the complex envelop of the optical signals. $b_0 = \omega_0 / 2Q_i + \omega_0 / 2Q_{e2} - \omega_0 / 2Q_{e1}$ and $a_0 = \omega_0 / 2Q_i + \omega_0 / 2Q_{e1} + \omega_0 / 2Q_{e2} = \omega_0 / 2Q = \Delta\omega_{3dB} /$

#217421 - $15.00 USD Received 21 Jul 2014; revised 17 Sep 2014; accepted 18 Sep 2014; published 17 Oct 2014

2 are the constant coefficients, with Q and $\Delta\omega_{3dB}$ denoting the quality factor and 3-dB angular bandwidth of the MRR, respectively. After simplification, Eq. (6) can be written as:

$$\frac{dy(t)}{dt} + a_0 y(t) = \frac{dx(t)}{dt} + b_0 x(t), \tag{7}$$

From Eq. (7), one can see that an add-drop MRR can be regarded as a linear first-order ODE system with coefficients of a_0 and b_0, which performs ODE solving for the complex envelop of optical signals. For high-speed optical signals on the order of GHz, the differential item dt is of the unit of picosecond. a_0 and b_0 determined by Q_i, Q_{e1}, and Q_{e2} of the add-drop MRR compensate the magnitude introduced by $1/dt$ on the order of 10^{12} Hz, allowing the proposed ODE solver to process high-speed optical signals.

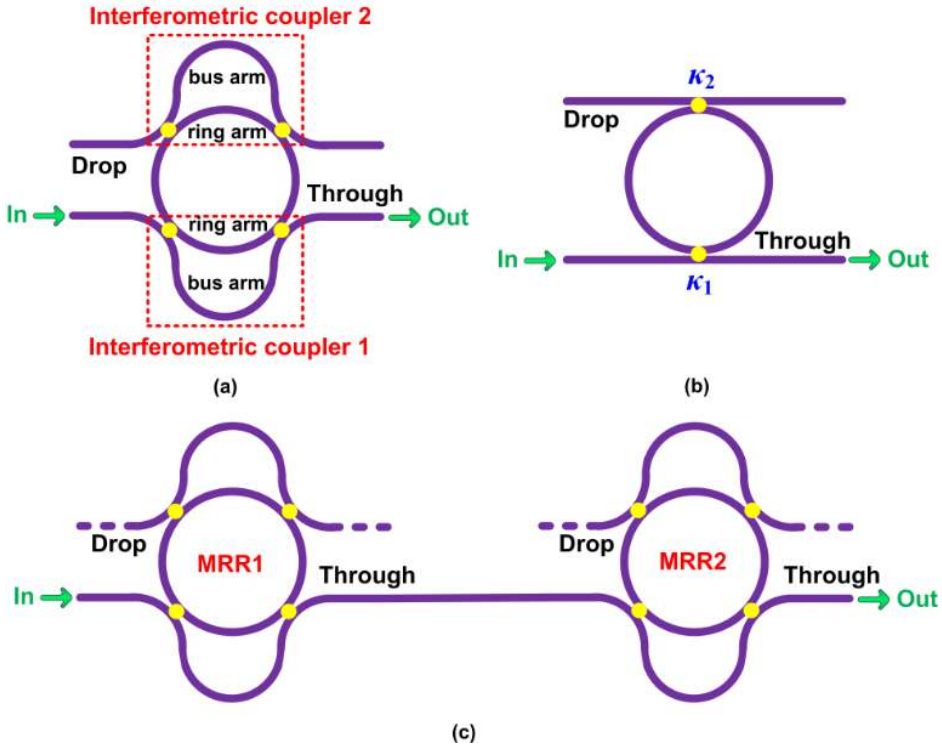

Fig. 1. (a) Schematic illustration of the proposed tunable first-order ODE solver based on an add-drop MRR with two interferometric couplers. (b) Add-drop MRR equivalent to (a) with two directional couplers. (c) Schematic illustration of the second-order ODE solver implemented by two cascaded add-drop MRRs with interferometric couplers.

Figure 1(a) illustrates the schematic configuration of our proposed tunable ODE solver, which consists of an add-drop MRR with two interferometric couplers 1 and 2. There are two arms in each interferometric coupler: one is the bus arm, and the other is the ring arm. The coupling strength between the microring and the input/drop waveguide can be dynamically changed by varying the phase shift along the bus arm of the interferometric coupler [18]. As a result, varied $Q_{e1,2}$ in Eq. (5) can be obtained, thus leading to tunable coefficients a_0 and b_0 of the ODE in Eq. (7). If one regards the interferometric couplers as equivalent directional couplers shown in Fig. 1(b), the effective power coupling coefficients of interferometric couplers 1 and 2 can be illustrated as:

$$\kappa_{1,2} = \kappa_0(1-\kappa_0)[T_{b1,2} + T_{r1,2} + 2\sqrt{T_{b1,2}T_{r1,2}}\cos(\varphi_{b1,2} - \varphi_{r1,2})], \tag{8}$$

#217421 - $15.00 USD Received 21 Jul 2014; revised 17 Sep 2014; accepted 18 Sep 2014; published 17 Oct 2014

where κ_0 is the power coupling coefficient at each coupling point in Fig. 1(a). $T_{b1,\,2}$ and $T_{r1,\,2}$ are the power transmission factors of the bus and ring arms of the two interferometric couplers, respectively. $\varphi_{b1,\,2} = \omega_0 n_{b1,\,2} L_{b1,\,2}/c$ and $\varphi_{r1,\,2} = \omega_0 n_{r1,\,2} L_{r1,\,2}/c$ are the phase shifts along the bus and ring arms of the two interferometric couplers, respectively, with $n_{b1,\,2}$ and $n_{r1,\,2}$ denoting the effective index of the bus and ring arms of the two interferometric couplers. Practically, φ_{b1} and φ_{b2} in Eq. (8) can be changed by tuning n_{b1} and n_{b2} through thermo-optic effect or electro-optic effect, thus leading to tunable coefficients a_0 and b_0 of the ODE in Eq. (7).

The proposed ODE solver can be extended to solve high-order differential equations by cascading more add-drop MRRs with tunable interferometric couplers. Consider the second-order ODE solver shown in Fig. 1 (c) as an instance, assuming that the two cascaded add-drop MRRs have a same resonance wavelength as the carrier frequency of input optical signal, the corresponding linear second-order ODE can be expressed as:

$$\frac{d^2 y(t)}{dt^2} + a_1 \frac{dy(t)}{dt} + a_0 y(t) = b_2 \frac{d^2 x(t)}{dt^2} + b_1 \frac{dx(t)}{dt} + b_0 x(t), \tag{9}$$

where the constant coefficients can be given by:

$$a_0 = a_{10} a_{20}, \quad a_1 = a_{10} + a_{20},$$
$$b_0 = b_{10} b_{20}, \quad b_1 = b_{10} + b_{20}, \quad b_2 = 1,$$

with a_{10}, b_{10} and a_{20}, b_{20} denoting the constant coefficients of the first-order ODEs corresponding to the two MRRs, respectively. Note that the second-order ODE in Eq. (9) also includes derivative terms of input signal that characterize general LTI systems, and various constant coefficients of the high-order ODE can be obtained by tuning the coefficients of the first-order ODEs corresponding to the individual MRRs.

3. Device design, fabrication, and characterization

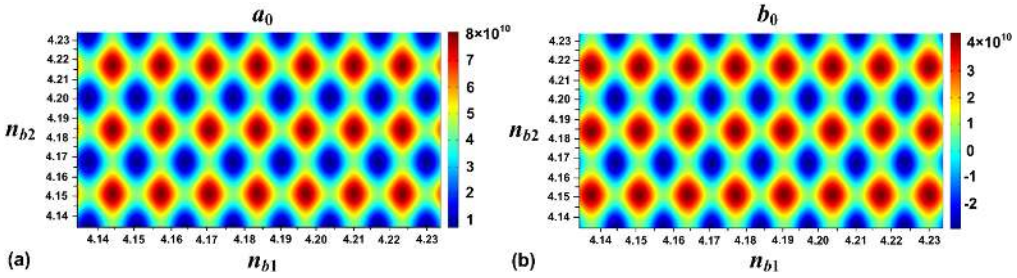

Fig. 2. Calculated coefficients (a) a_0 and (b) b_0 of the ODE in Eq. (7) for various n_{b1} and n_{b2}.

The structural parameters of the proposed device are chosen as follows: the gap size in the coupling region is 0.18 μm due to the resolution limitation of deep ultraviolet (DUV) photolithography used in our fabrication. The straight coupling length of the directional coupler at each coupling point in Fig. 1(a) is 2.50 μm to enhance the coupling by increasing the interaction length. Stronger coupling means larger κ_0 in Eq. (8), thus leading to broader tuning ranges of coefficients a_0 and b_0 in Eq. (7). The circumference of the microring is L = 178.98 μm, which is a trade-off between the device footprint and the implementation of the interferometric couplers. The physical lengths of the bus and ring arms of the two interferometric couplers are L_{b1} = 116.80 μm, $L_{r1} = L_{b2} = L_{r2}$ = 47.12 μm, respectively. Here we choose two interferometric couplers with different physical lengths of bus arms to compare tuning effects. Longer bus arms can also improve the tuning efficiencies of the thermo-optic microheaters along them. For single-mode silicon photonic waveguides with a cross section of 450 × 220 nm^2, the calculated power coupling coefficient of each directional coupler using Lumerical finite-difference time-domain (FDTD) solutions is κ_0 = 0.0441. We

#217421 - $15.00 USD Received 21 Jul 2014; revised 17 Sep 2014; accepted 18 Sep 2014; published 17 Oct 2014

also assume that the waveguide group index of the transverse electric (TE) mode is $n_g = n_{r1} = n_{r2} = 4.1850$, and the waveguide power loss factor is $\alpha = 8$ dB/cm based on our previously fabricated devices. Figures 2(a) and 2(b) present the calculated coefficients a_0 and b_0 in Eq. (7) for various n_{b1} and n_{b2} using the above design parameters, respectively. It can be seen that, by changing the effective index of the bus arms, the proposed device can be used to solve ODE in Eq. (7) with varied coefficients a_0 and b_0.

The designed device based on the above principle was fabricated on an 8-inch SOI wafer with 220-nm-thick top silicon layer and 2-μm-thick buried oxide (BOX) layer. The micrograph of the fabricated device is shown in Fig. 3(a). 248-nm DUV photolithography was utilized to define the device layout, and inductively coupled plasma (ICP) etching process was used to etch the top silicon layer. Grating couplers for TE polarization were employed at the ends of the input/output port to couple light into/out of the chip with single mode fibers (SMFs). The drop port is also connected to a grating coupler to dissipate the undesired signal with negligible reflection. After etching of the waveguides and grating couplers, a 1.5-μm-thick silica layer was deposited on the top silicon layer as a separation layer by plasma enhanced chemical vapor deposition (PECVD). Then a 200-nm-thick TiN layer was sputtered on the separation layer and TiN heaters along the bus arms of the two interferometric couplers were fabricated using DUV photolithography and dry etching. Via holes were opened after further deposition of a 300-nm-thick silica layer by PECVD, followed by the fabrication of the aluminum wires and pads. The entire fabrication process is CMOS compatible. The TiN microheaters were only placed along the bus arms of the two interferometric couplers in order to tune the effective index through thermo-optic effect without shifting the resonance wavelengths of the add-drop MRR.

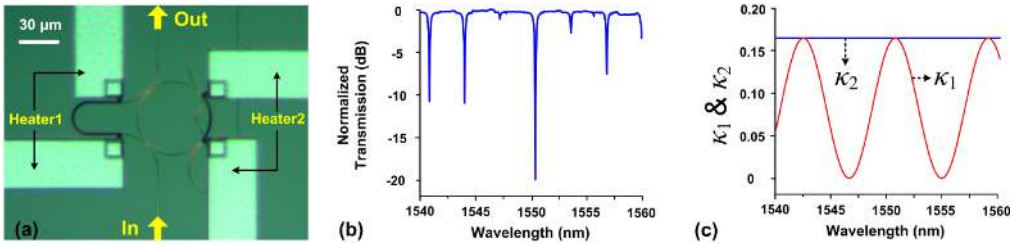

Fig. 3. (a) Micrograph of the fabricated device. (b) Experimentally measured through port transmission spectrum of the fabricated device. (c) Simulated effective power coupling coefficients $\kappa_{1,2}$ in the 1540 nm ~1560 nm wavelength range.

The normalized transmission spectrum of the through port measured with the fabricated device is shown in Fig. 3(b). The on-chip insertion loss is ~10.5 dB, which is mainly attributed to the coupling loss induced by the vertical coupling system. The resonance notches with various depths and bandwidths in Fig. 3(b) are attributed to wavelength dependence of κ_1 in Eq. (8), as illustrated in Fig. 3(c). Since the bus and ring arms of interferometric coupler 2 have the same physical length, i.e., $L_{b2} = L_{r2} = 47.12$ μm, κ_2 in Eq. (8) remains unchanged for different wavelengths.

#217421 - $15.00 USD Received 21 Jul 2014; revised 17 Sep 2014; accepted 18 Sep 2014; published 17 Oct 2014

4. System testing of solving ODE with tunable coefficients

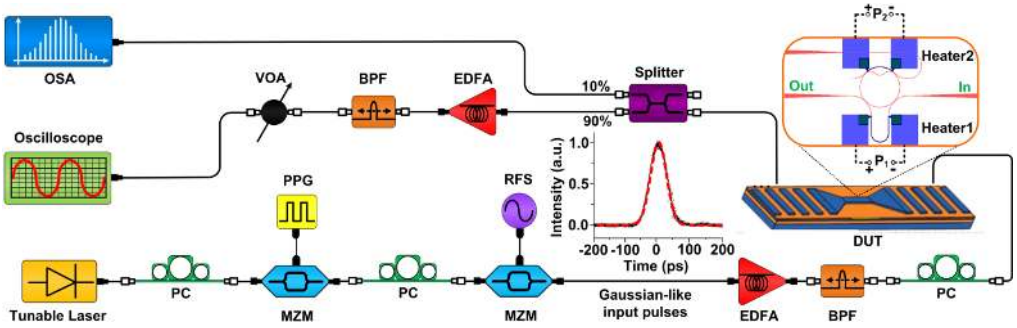

Fig. 4. Experimental setup for system testing of solving ODE with tunable coefficients. PC: polarization controller. MZM: Mach-Zehnder modulator. PPG: pulse pattern generator. RFS: radio frequency synthesizer. EDFA: erbium-doped fiber amplifier. BPF: band pass filter. DUT: device under test. VOA: variable optical attenuator. OSA: optical spectrum analyzer. The experimentally observed 10-Gb/s optical Gaussian-like input pulse and the fitted one are shown in the inset by the black solid and red dashed curves, respectively.

We use the experimental setup shown in Fig. 4 to test the performance of the fabricated device as a tunable first-order photonic ODE solver. The wavelength of the continuous-wave (CW) light launched by a tunable laser with a tuning resolution of 0.001 nm is set to 1550.391 nm, which is one of the resonance wavelengths in Fig. 3(b). Optical Gaussian-like pulses as shown in Fig. 4 are chosen as typical input pulse waveforms in our experiment. The Gaussian-like pulses are generated by two cascaded Mach-Zehnder modulators (MZMs) [20]. The first MZM is driven by a 10-Gb/s non-return-to-zero (NRZ) signal generated from a pulse pattern generator (PPG) with a pattern of "10000000", and the second one performs as a pulse carver driven by a 10-GHz radio frequency signal from a radio frequency synthesizer (RFS). An erbium-doped fiber amplifier (EDFA) is utilized to boost the generated signal, followed by a tunable band pass filter (BPF) to suppress the amplified spontaneous emission (ASE) noise. A polarization controller (PC) is inserted before the device under test (DUT) to make sure that the input signal is TE polarized. The output signal from the DUT is split into two parts by a 90:10 fiber splitter. One part is fed into the optical spectrum analyzer (OSA), and the other part is amplified by another EDFA with one more BPF to suppress the ASE noise. After going through a variable optical attenuator (VOA), the temporal waveforms are recorded by an oscilloscope.

According to previous discussion, various coefficients a_0 and b_0 of the ODE in Eq. (7) can be obtained by changing n_{b1} or n_{b2} in Figs. 2(a) and 2(b). In our experiment, the changing of n_{b1} and n_{b2} is realized by tuning the heating powers P_1 and P_2 applied to Heater 1 and 2 in Fig. 4, respectively. We perform four sets of system testing with (1) varied P_1 and unchanged P_2, (2) varied P_2 and unchanged P_1, (3) varied b_0 and constant a_0, and (4) varied a_0 and constant b_0. The first and second sets of system testing are used to test the TiN microheaters and demonstrate the tunability of the fabricated device. In these two sets, both coefficients a_0 and b_0 are changed with varied P_1 or P_2. In practical applications, it may be required to change only one of the two coefficients. Therefore we perform the third and fourth sets of system testing with only one of the two constant coefficients varied by accurately tuning both P_1 and P_2. For each set, we perform three testings I ~III with different P_1 or P_2 for comparisons. In our experiment, the observed transmission spectra and output pulse waveforms can remain stable for ~5 minutes in room temperature when the heating power applied to the TiN microheaters is lower than 20 mW. For all the four sets of system testing, the redshift of the resonance wavelength at 1550.391 nm is smaller than 0.15 nm. In order to achieve accurate alignment with the resonance wavelength of the fabricated device, the output pulse waveforms are recorded only when the power of the output signal reaches a minimum during the fine tuning process of the CW light around ~1550.391 nm.

#217421 - $15.00 USD Received 21 Jul 2014; revised 17 Sep 2014; accepted 18 Sep 2014; published 17 Oct 2014

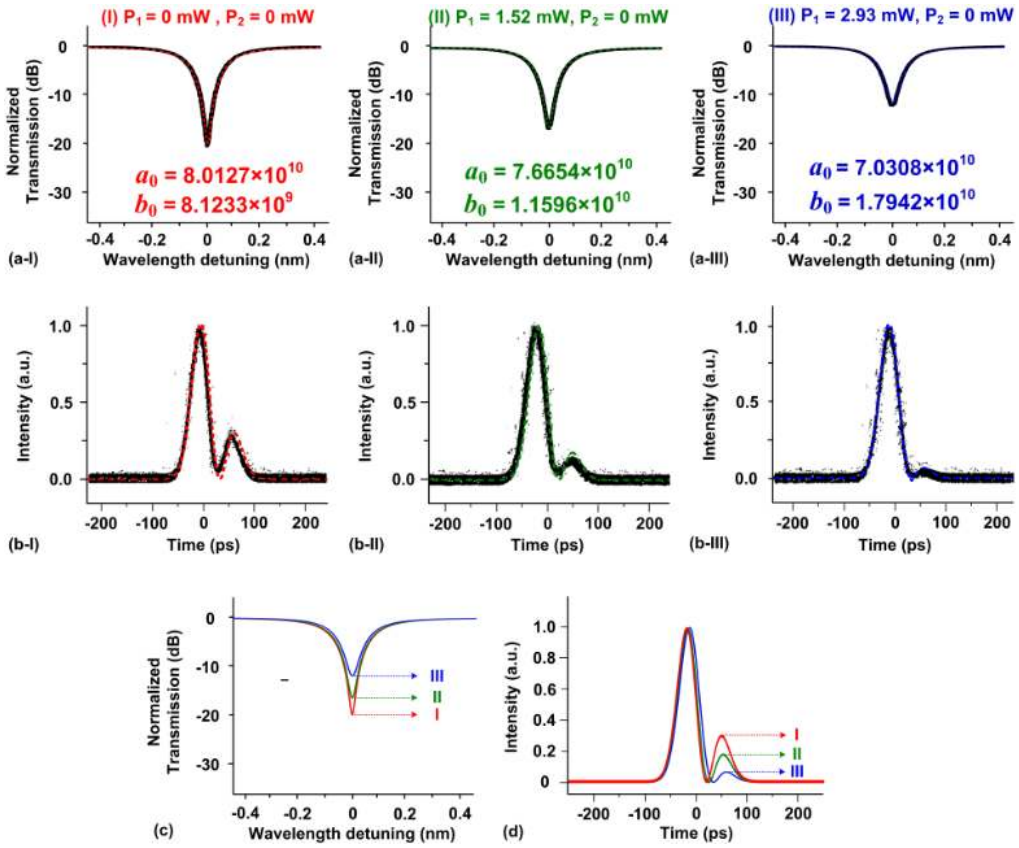

Fig. 5. Experimental results of the first set of system testing with varied P_1 and unchanged P_2. (a-I)–(a-III) Measured (solid curves) and fitted (dashed curves) transmission spectra of testings I, II, and III, respectively. (b-I)–(b-III) Experimentally observed temporal output pulse waveforms (solid curves) and numerical solutions of the ODE in Eq. (7) with fitted coefficients a_0 and b_0 in (a-I)–(a-III) (dashed curves), respectively. (c)–(d) Fitted transmission spectra and numerical solutions of the ODE in Eq. (7) for the three testings, respectively.

For the first set of system testing with varied P_1 and unchanged $P_2 = 0$ mW, the measured transmission spectra and experimentally observed output pulse waveforms are shown in Figs. 5(a-I)–5(a-III) and Figs. 5(b-I)–5(b-III) by the solid curves, respectively. The fitted spectra and numerical solutions of the ODE in Eq. (7) with fitted coefficients a_0 and b_0 are represented by the dashed curves accordingly. The fitted coefficients a_0 and b_0 are obtained from the fitted spectra in Figs. 5(a-I)–5(a-III), respectively. The amplitudes of the output pulses are normalized for easier comparisons. It can be seen that the observed output waveforms in Figs. 5(b-I)–5(b-III) match closely with the numerical solutions of the ODE in Eq. (7). To make qualitative comparisons, the fitted spectra and numerical solutions for testings I, II, and III are plotted in Figs. 5(c) and 5(d), respectively. One can see that by tuning P_1, both a_0 and b_0 can vary, thus leading to various output pulse waveforms corresponding to the solutions of the ODE in Eq. (7) with different coefficients.

#217421 - $15.00 USD Received 21 Jul 2014; revised 17 Sep 2014; accepted 18 Sep 2014; published 17 Oct 2014

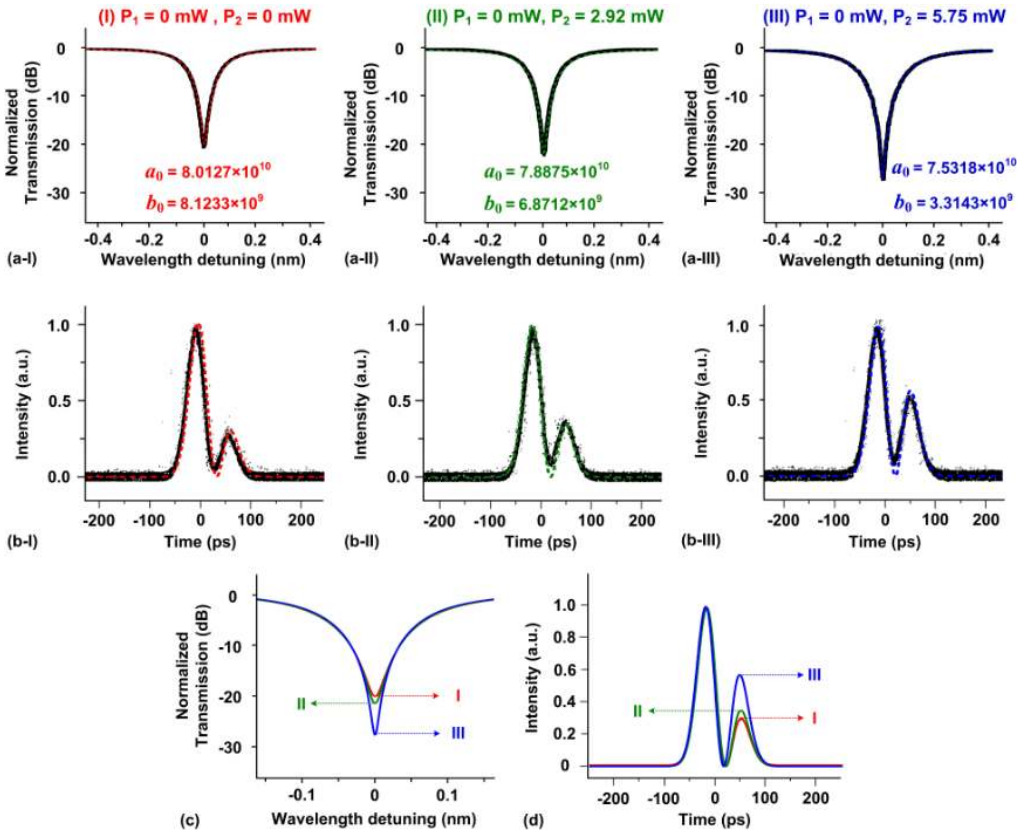

Fig. 6. Experimental results of the second set of system testing with unchanged P_1 and varied P_2. (a-I)–(a-III) Measured (solid curves) and fitted (dashed curves) transmission spectra of testings I, II, and III, respectively. (b-I)–(b-III) Experimentally observed temporal output pulse waveforms (solid curves) and numerical solutions of the ODE in Eq. (7) with fitted coefficients a_0 and b_0 in (a-I)–(a-III) (dashed curves), respectively. (c)–(d) Fitted transmission spectra and numerical solutions of the ODE in Eq. (7) for the three testings, respectively.

Similar to the first set of system testing, the measured and fitted transmission spectra of testings I, II, and III in the second set of system testing with varied P_2 and unchanged $P_1 = 0$ mW are shown in Figs. 6(a-I)–6(a-III), respectively. The experimentally observed output pulse waveforms, as well as the numerical solutions of the ODE in Eq. (7) for the three testings, are shown Figs. 6(b-I)–6(b-III), respectively. The observed output waveforms also show good agreement with the numerical solutions of the ODE in Eq. (7) with fitted coefficients a_0 and b_0 obtained from the fitted spectra in Figs. 6(a-I)–6(a-III). The fitted spectra and numerical solutions for the three testings are illustrated in Figs. 6(c) and 6(d), respectively. By tuning P_2, one can also obtain various output pulse waveforms corresponding to the solutions of the ODE in Eq. (7) with both a_0 and b_0 changed.

#217421 - $15.00 USD Received 21 Jul 2014; revised 17 Sep 2014; accepted 18 Sep 2014; published 17 Oct 2014

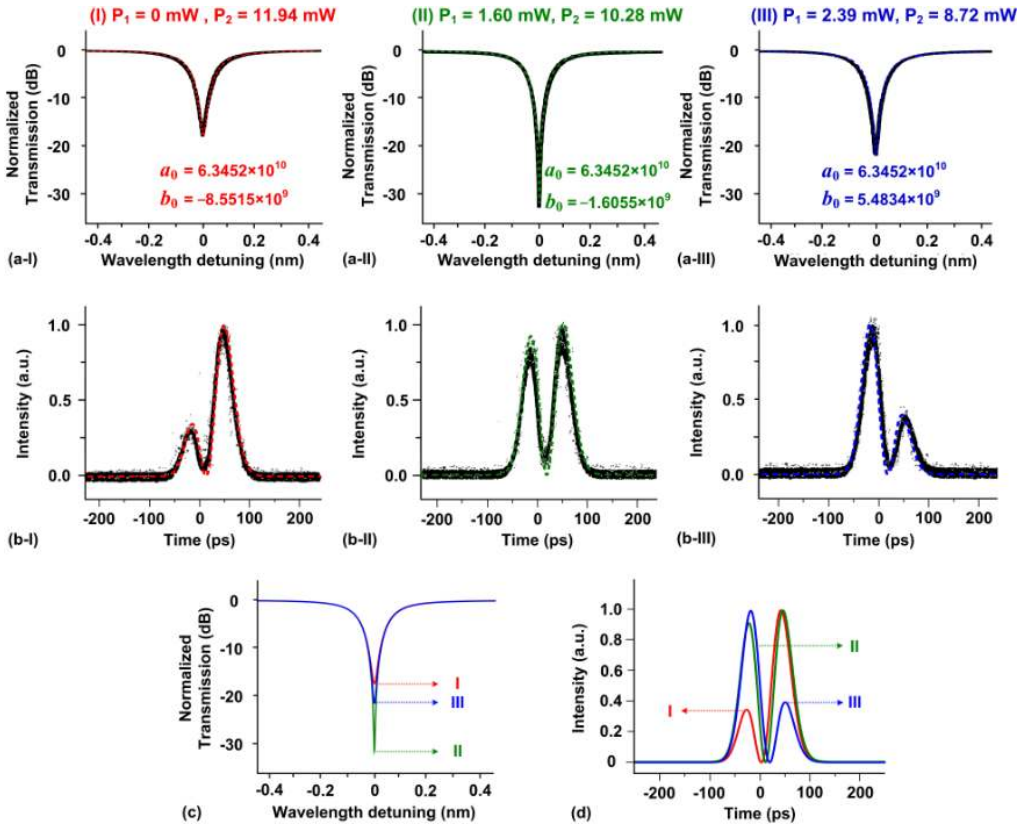

Fig. 7. Experimental results of the third set of system testing with constant a_0 and varied b_0. (a-I)–(a-III) Measured (solid curves) and fitted (dashed curves) transmission spectra of testings I, II, and III, respectively. (b-I)–(b-III) Experimentally observed temporal output pulse waveforms (solid curves) and numerical solutions of the ODE in Eq. (7) with fitted coefficients a_0 and b_0 in (a-I)–(a-III) (dashed curves), respectively. (c)–(d) Fitted transmission spectra and numerical solutions of the ODE in Eq. (7) for the three testings, respectively.

For the third set of system testing with varied b_0 and constant $a_0 = 6.3452 \times 10^{10}$, the measured transmission spectra and experimentally observed output pulse waveforms are shown in Figs. 7(a-I)–7(a-III) and Figs. 7(b-I)–7(b-III) by the solid curves, respectively. The fitted spectra and numerical solutions of the ODE in Eq. (7) with fitted coefficients a_0 and b_0 are represented by the dashed curves accordingly. The fitted spectra and numerical solutions for the three testings are illustrated in Figs. 7(c) and 7(d), respectively. The value of b_0 can be either positive or negative, depending on the coupling regime of the MRR [21]. For the fourth set of system testing, the measured and fitted transmission spectra for testings I, II, and III with varied a_0 and constant $b_0 = 6.7874 \times 10^9$ are shown in Figs. 8(a-I)–8(a-III), respectively. The experimentally observed output pulse waveforms, as well as the numerical solutions of the ODE in Eq. (7) for testings I, II, and III, are shown Figs. 8(b-I)–8(b-III), respectively. The fitted spectra and numerical solutions of the three testings are illustrated in Figs. 8(c) and 8(d), respectively. It can be seen that the output pulse waveforms also fit well with the numerical solutions of the ODE in Eq. (7) for the third and fourth sets of system testing. By properly tuning both P_1 and P_2, one can obtain solutions of the ODE in Eq. (7) with only one of the two coefficients a_0 and b_0 changed. The agreement between the output pulse waveforms and the numerical solutions of the ODE for all the four sets of system testing verifies the effectiveness of the proposed device as a tunable photonic ODE solver.

#217421 - $15.00 USD Received 21 Jul 2014; revised 17 Sep 2014; accepted 18 Sep 2014; published 17 Oct 2014

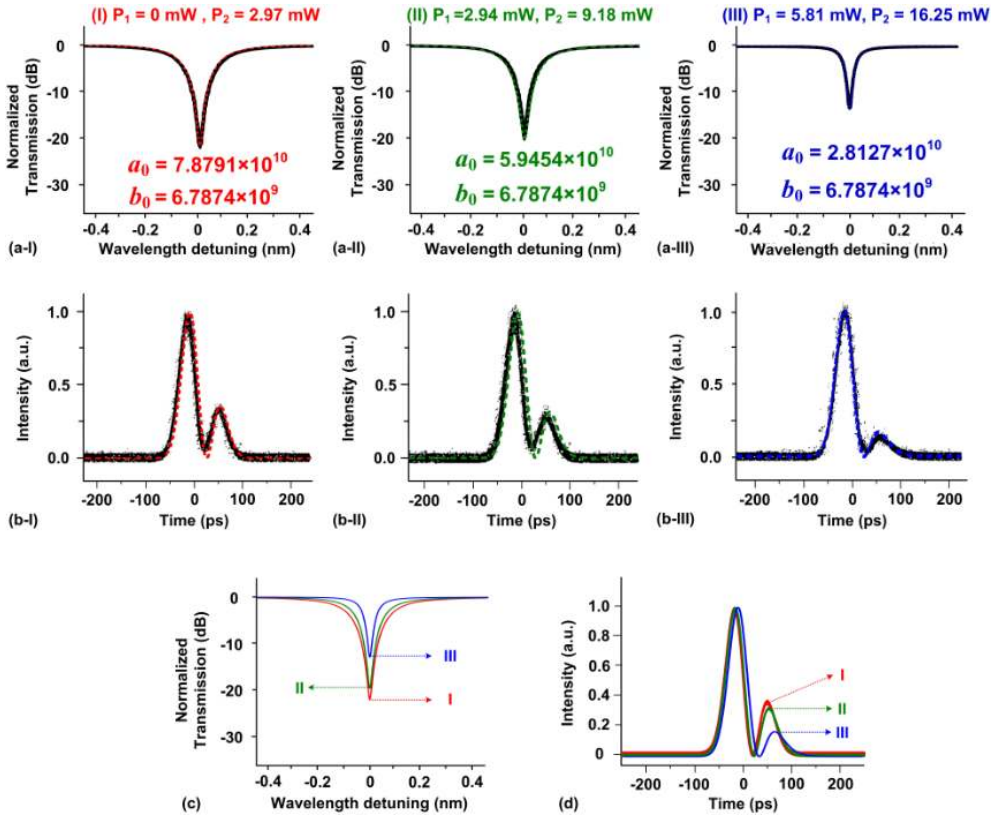

Fig. 8. Experimental results of the fourth set of system testing with varied a_0 and constant b_0. (a-I)–(a-III) Measured (solid curves) and fitted (dashed curves) transmission spectra of testings I, II, and III, respectively. (b-I)–(b-III) Experimentally observed temporal output pulse waveforms (solid curves) and numerical solutions of the ODE in Eq. (7) with fitted coefficients a_0 and b_0 in (a-I)–(a-III) (dashed curves), respectively. (c)–(d) Fitted transmission spectra and numerical solutions of the ODE in Eq. (7) for the three testings, respectively.

5. Conclusion

In summary, we have proposed and experimentally demonstrated a tunable all-optical temporal differential-equation solver capable of solving ODEs with derivative terms of input signal that characterizes general LTI systems. The photonic device based on an add-drop MRR with two tunable interferometric couplers is monolithically integrated on a SOI platform with a compact footprint of ~60 μm × 120 μm. By thermally tuning the phase shifts along the bus arms of the two interferometric couplers, the proposed device can be used to solve first-order ODEs with two variable coefficients. The performance of the fabricated device as an effective tunable ODE solver has been tested by four sets of system testing using 10-Gb/s optical Gaussian-like pulses. The compact footprint, high processing speed, and CMOS-compatible fabrication process, together with reconfigurability and scalability are all key attributes required for on-chip processors, making the proposed ODE solver a promising candidate in future all-optical computing and information processing systems.

Acknowledgments

This research was supported in part by the National Natural Science Foundation of China under Grant 61125504/61235007, and in part by the 863 High-Tech Program under Grant 2013AA013402. We also acknowledge IME Singapore for device fabrication.

#217421 - $15.00 USD Received 21 Jul 2014; revised 17 Sep 2014; accepted 18 Sep 2014; published 17 Oct 2014